Check for updates

JGR Space Physics

RESEARCH ARTICLE
10.1029/2024JA033285

Excitation of Upper-Hybrid and Whistler-Mode Waves by Electron Velocity Ring Distribution

Sang-Yun Lee[1,2] **and Peter H. Yoon**[3]

[1]NASA Goddard Space Flight Center, Greenbelt, MD, USA, [2]Department of Physics, The Catholic University of America, Washington, DC, USA, [3]Institute for Physical Science and Technology, University of Maryland, College Park, MD, USA

Key Points:

- Quasi-electrostatic upper-hybrid wave accompanied by electron Bernstein modes are excited by electron velocity ring distribution
- Over longer time interval quasi-parallel whistler waves are excited, which lead to the formation of partial velocity shell distribution
- Particle-in-cell simulation results are interpreted by quasilinear theory

Correspondence to:
S.-Y. Lee,
sangyun.lee@nasa.gov

Citation:
Lee, S.-Y., & Yoon, P. H. (2025). Excitation of upper-hybrid and whistler-mode waves by electron velocity ring distribution. *Journal of Geophysical Research: Space Physics*, *130*, e2024JA033285. https://doi.org/10.1029/2024JA033285

Received 12 SEP 2024
Accepted 31 JAN 2025

Abstract The magnetospheres of the Earth and other magnetized planets are replete with high-frequency fluctuations, which are sometimes accompanied by multiple-harmonic electron cyclotron waves, and lower frequency waves of the whistler-mode type. Such waves are presumed to be excited by energetic electrons trapped in the dipolar magnetic field, the so-called loss-cone electrons, the electron ring distribution being a highly idealized example. The present paper investigates the stability of electron ring distribution with respect to the excitation of quasi-electrostatic upper-hybrid wave instability as well as the quasi-electromagnetic whistler mode instability that operates near electron cyclotron frequency. By employing a two-dimensional particle-in-cell numerical simulation, it is demonstrated that the relatively early dynamics is dominated by the upper-hybrid wave instability, but over a longer time period it is the whistler mode instability that ultimately determines the final relaxed state. The simulation results are interpreted with the quasilinear theoretical framework.

1. Introduction

Magnetospheres of planets with internal magnetic fields are a rich source of radio and plasma waves. Among the vast array of wave phenomena that characterize such magnetospheres during the relatively quiet-time conditions, the quasi electrostatic fluctuations with peak frequency in the upper-hybrid frequency range are pervasively detected, a wave phenomenon that had been known since the early days of in situ space exploration (Christiansen et al., 1978a, 1978b; Kurth, Craven, et al., 1979, Kurth, Ashour-Abdalla, et al., 1979; Kurth et al., 2015; Matsumoto & Usui, 1997; Usui et al., 1999). Such upper-hybrid range fluctuations are often accompanied by multiple-harmonic electron-cyclotron frequency emissions, which are often interpreted as electron Bernstein modes. In addition to these quasi-electrostatic fluctuations, the magnetospheric environment is also characterized by quasi-electromagnetic whistler-mode type of wave phenomena (Artemyev et al., 1978; Cully et al., 2008; Helliwell, 1969). The whistler-mode type of waves are also pervasively observed in other magnetized planetary systems such as the Jovian magnetosphere, as recently reported (Ma et al., 2024; Menietti et al., 2021; Zhang et al., 2020) The auroral ionosphere and the magnetopause region of the Earth are also sources of plentiful wave activities and radio emissions (LaBelle & Treumann, 1988, 2006; LaBelle et al., 2005; Weatherwax et al., 1995). The free energy source for these emissions are presumed to be associated with the loss-cone feature in the energetic electron velocity distribution function (VDF), which forms as a result of trapped electrons bouncing back and forth in the inhomogeneous dipolar magnetic field, and undergoing mirror reflection at low altitudes of both polar ends (Davidson & Walt, 1977; Summers et al., 2004). The electron perpendicular ring distribution may be conceived of as an extreme example of the loss-cone distribution in that the loss-cone distribution is characterized by a perpendicular population inversion feature, which the ring distribution also possesses. It should be pointed out that the adoption of an electron ring distribution is meant as a highly-idealized form of the loss-cone distribution rather than as representing actual observations. Nevertheless, such a model can be realized in actual situations, albeit briefly in time, for example, as in the ionospheric heating experiment by powerful ground-based radio waves (Eliasson et al., 2016; Grach, 1999). In the present paper, we investigate the physical processes relevant to the electron ring VDF. Let us first briefly overview the relevant literature in this regard.

As noted, the electron ring distribution leads to the excitation of electrostatic upper-hybrid waves and electron Bernstein modes (Eliasson et al., 2016). The electron Bernstein waves interact with electrons with wave frequency at the Doppler shifted electron cyclotron resonance frequency and its harmonics (Ram et al., 2002) and play an important role in electron dynamics of radiation belt and ring current in the Earth's magnetosphere. For example, electron cyclotron harmonic (ECH) wave in the Earth's magnetosphere is a famous example of electron Bernstein waves at multiple frequency ranges at $(n + 1/2)f_{ce}$, where $f_{ce} = (eB_0)/(2\pi m_e c)$ is the electron gyro

© 2025. American Geophysical Union. All Rights Reserved.

21699402, 2025, 2, Downloaded from https://agupubs.onlinelibrary.wiley.com/doi/10.1029/2024JA033285 by University Of Maryland, Wiley Online Library on [14/02/2025]. See the Terms and Conditions (https://onlinelibrary.wiley.com/terms-and-conditions) on Wiley Online Library for rules of use; OA articles are governed by the applicable Creative Commons License

frequency. Here, e is unit electric charge, B_0 is the magnitude of background magnetic field, m_e is the mass of an electron, and c is the speed of light. ECH waves are mainly excited at the night sector and responsible for scattering electrons near the loss cone (Thorne et al., 2010). Recently, large-amplitude electron Bernstein waves have been observed at the upper-hybrid frequency range, which led Li et al., 2020 to speculate that these waves contribute to the cross-field diffusion by thermalizing and diffusing electrons around the electron diffusion region.

The electron ring distribution may also excite electromagnetic waves since the perpendicular ring feature provides the effective perpendicular temperature anisotropy. Consequently, it may lead to the excitation of whistler-anisotropy instability (Gary & Wang, 1996). For sufficiently strongly magnetized plasma, or equivalently, for sufficiently low electron density, the ring distribution with its perpendicular population inversion feature, $\partial f/\partial v_\perp > 0$, where f represents the VDF, may lead to a direct emission of electromagnetic radiation via relativistic cyclotron maser instability (CMI) (Lee et al., 2013). The cyclotron maser mechanism is known as responsible for the Earth's auroral kilometric radiation (AKR) (Wu & Lee, 1979). In the literature, simulations of electron cyclotron maser emission (ECME) have been carried out for low-density, highly magnetized plasma conditions typical of the AKR source region (Pritchett, 1984a, 1984b, 1986, 1999; Pritchett & Winglee, 1989; Pritchett & Strangeway, 1985). While the cyclotron maser emission mechanism is largely discussed in the literature in the context of the planetary radio emission such as AKR, some recent literature also discuss its applicability in the context of the solar radio bursts, particularly, the solar type III radio emissions (Ni et al., 2020; Wu et al., 2000; Yoon et al., 2002). Note, however, that CMI ceases to operate if the plasma density is sufficiently high, or the magnetic field is sufficiently low. In general the CMI condition for the fundamental electron cyclotron frequency, $f \sim f_{ce}$, requires the ratio of plasma frequency to electron gyro frequency, f_{pe}/f_{ce}, to be less than 0.1 or so, where $f_{pe} = \sqrt{(n_0 e^2)/(\pi m_e)}$ is the electron plasma frequency, n_0 being the ambient plasma density.

With this brief overview, we now proceed to discuss the purview of the present paper. We are interested in the plasma instabilities excited by an electron ring distribution under the condition where the ratio of electron plasma frequency to the gyro frequency is sufficiently high, of the order, between $\mathcal{O}(1)$ to $\mathcal{O}(10)$ or so. Such a condition may be representative of a typical magnetospheric condition such as the near-Earth nightside equatorial magnetotail region. The quasi-electrostatic Bernstein/upper-hybrid waves excited by the ring distribution function under such a condition was studied recently by Lee et al. (2018) and Yoon and Omura (2023) with the assumption of exactly perpendicular propagation of waves with respect to the ambient magnetic field, and by employing a one-dimension (1D) electrostatic particle-in-cell (PIC) simulation, combined with a quasilinear theory. Similarly, Yoon et al. (2019) investigated the parallel electromagnetic whistler-mode instability excited by the electron ring distribution, with the 1D PIC code plus quasilinear theory. Umeda et al. (2007), on the other hand, carried out a two-dimensional (2D) non-relativistic PIC simulation of the combined upper-hybrid and whistler mode instabilities. Against this backdrop, we revisit these previous works (Lee et al., 2018; Umeda et al., 2007; Yoon & Omura, 2023; Yoon et al., 2019) by employing a relativistic 2D PIC code simulation, and interpreting the result with quasilinear theory. As noted, while Umeda et al. (2007) have already accomplished the task of 2D PIC code simulation of the electron ring distribution, their simulation is based on the non-relativistic formalism, while the present paper utilizes the fully relativistic code. One of the main differences between the non-relativistic versus relativistic schemes is that the non-relativistic wave-particle resonance is strictly forbidden for exactly perpendicular propagation, and thus, the excitation of purely perpendicular Bernstein/upper-hybrid modes is not possible within the non-relativistic framework. Moreover, while Lee et al. (2018), Yoon and Omura (2023) and Yoon et al. (2019) have carried out the 1D PIC code simulations for the two extreme limits of exactly perpendicular and parallel propagations, the combined 2D simulation has not been done within the context of the relativistic formalism. Also, it was not clear whether the quasilinear theories developed in these works, which pertained to the two limiting cases still hold valid when the fully 2D dynamics is simulated. For these reasons, we revisit the same problem of ring beam distribution by employing the relativistic 2D PIC simulation and (re)interpreting the result with quasilinear theory.

The organization of this paper is as follows: In Section 2 we describe the simulation environment and setup. Section 3 presents the simulation result, together with the detailed diagnosis. Section 4 is devoted to the interpretation of the 2D PIC simulation by means of quasilinear theory. This section is further divided in to subsections. Section 4.1 pertains to the quasilinear analysis for upper-hybrid instability, which is followed by

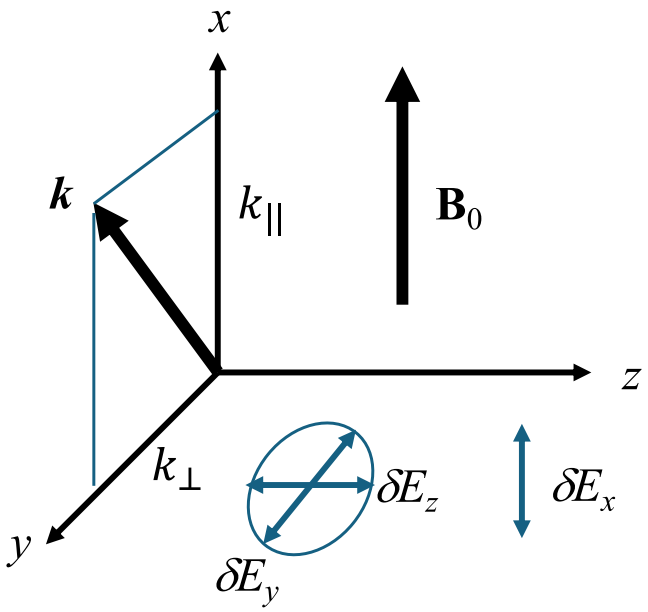

Figure 1. The basic geometrical configuration of the present study. The simulation is carried out in the xy plane. The wave electric field vector elements δE_y and δE_z depict the right-hand circular whistler-mode polarization in the case of quasi-parallel mode, while for quasi-perpendicular propagation, the dominant δE_y denotes the quasi-electrostatic upper-hybrid mode polarization.

Section 4.2 where the longer term whistler mode instability development is modeled with the quasilinear theory. Finally Section 5 concludes the present paper with the summary and discussion.

2. Simulation Setting

We employed a two-dimensional (2D) relativistic and electromagnetic particle-in-cell (PIC) code (Lee et al., 2015) to simulate the dynamics of the electron perpendicular ring velocity distribution and its evolution in response to the excitation of instabilities. The system sizes along x and y-directions are $L_x = L_y \sim 1448\lambda_{De}$, where $\lambda_{De} = \sqrt{T_e/(4\pi n_0 e^2)}$ is electron Debye length, which corresponds to the number of grids being equal to $N_x = N_y = 1024$ and with a grid size of $\Delta x = \Delta y = \sqrt{2}\lambda_{De}$. Here, T_e is the electron temperature. The number of particles is 256 per grid and for each species (protons and electrons). We have adopted the realistic proton-to-electron mass ration, $m_i/m_e = 1836$. The protons do not play much dynamical role because of the fact that we are interested in the rapid dynamics of electrons and high-frequency waves. We used three species in this simulation: the protons, background electrons, and perpendicular ring distribution of energetic electrons. The ring population consists of 10% of the total electron content, namely, $n_b/n_0 = 0.1$, where n_b is the ring electron number density. The background magnetic field is directed along positive x-direction with the plasma to gyro-frequency ratio equal to $\omega_{pe}/\Omega_{ce} = 10$. Here, $\omega_{pe} = 2\pi f_{pe}$ and $\Omega_{ce} = 2\pi f_{ce}$ are angular frequencies. The electron thermal speed is $v_{th,\,e}/c = 1/40$ for both background and ring electrons, and protons have the same temperature as that of the electrons. The boundary conditions are periodic for both x- and y-directions.

Figure 1 schematically depicts the basic geometry associated with the present investigation. The simulation is carried out in xy plane, and the ambient magnetic field directed along the positive x axis is shown with a thick arrow, $\mathbf{B}_0 = B_0\hat{\mathbf{x}}$. The wave vector lies along the simulation plane, $\mathbf{k} = k_\perp\hat{\mathbf{y}} + k_\parallel\hat{\mathbf{x}}$. All three electric field vector components are shown, but we display δE_y and δE_z together as if they form an elliptical polarization. For purely parallel propagation, $\mathbf{k} = k_\parallel\hat{\mathbf{x}}$, the wave electric field vector $\delta\mathbf{E}_\perp = \delta E_y\hat{\mathbf{y}} \pm \delta E_z\hat{\mathbf{z}}$ represents the right/left-hand circular polarization, while for the purely perpendicular propagation, $\mathbf{k} = k_\perp\hat{\mathbf{y}}$, the wave electric field vector $\delta\mathbf{E}_\perp = \delta E_y\hat{\mathbf{y}} + \delta E_z\hat{\mathbf{z}}$ depicts the extraordinary mode polarization. The quasi-parallel whistler mode is characterized by the quasi right-hand mode, while the quasi-perpendicular and quasi-electrostatic upper-hybrid mode is characterized by the dominant δE_y polarization. These properties will be verified by the subsequent simulation result. For quasi-parallel propagation, the electric field component δE_x represents the longitudinal electrostatic mode, while for quasi-perpendicular propagation δE_x corresponds to the ordinary mode polarization. The corresponding wave magnetic field can be deduced from Faraday's law, $c\mathbf{k}\times\delta\mathbf{E} = \omega\delta\mathbf{B}$, or $\delta B_x = (ck_\perp/\omega)\delta E_z$, $\delta B_y = -(ck_\parallel/\omega)\delta E_z$, and $\delta B_z = (c/\omega)(k_\parallel\delta E_y - k_\perp\delta E_x)$.

3. Simulation Results

The result of 2D PIC simulation is plotted in Figure 2. The relatively early dynamics is dominated by the excitation of δE_y field, with a much weaker δE_x field excitation. The z component electric field is extremely low. As will be shown in more detail, the y component wave electric field excitation corresponds to the quasi-perpendicular and quasi-electrostatic upper-hybrid mode, accompanied by weak multiple-harmonic electron cyclotron (Bernstein) modes. The longer time-scale dynamics is dictated by the y and z component magnetic wave fields, which are combined as $(\delta B_y^2 + \delta B_z^2)/2$. This combined field turns out to correspond to the quasi-parallel and quasi-electromagnetic whistler (or electron cyclotron) mode waves. The x component wave magnetic field is also very low. Recall that δB_x and δE_z are related to each other by the relationship $\delta B_x = (ck_\perp/\omega)\delta E_z$ such that it is not surprising that their temporal variations mirror each other.

21699402, 2025, 2, Downloaded from https://agupubs.onlinelibrary.wiley.com/doi/10.1029/2024JA033285 by University Of Maryland, Wiley Online Library on [14/02/2025]. See the Terms and Conditions (https://onlinelibrary.wiley.com/terms-and-conditions) on Wiley Online Library for rules of use; OA articles are governed by the applicable Creative Commons License

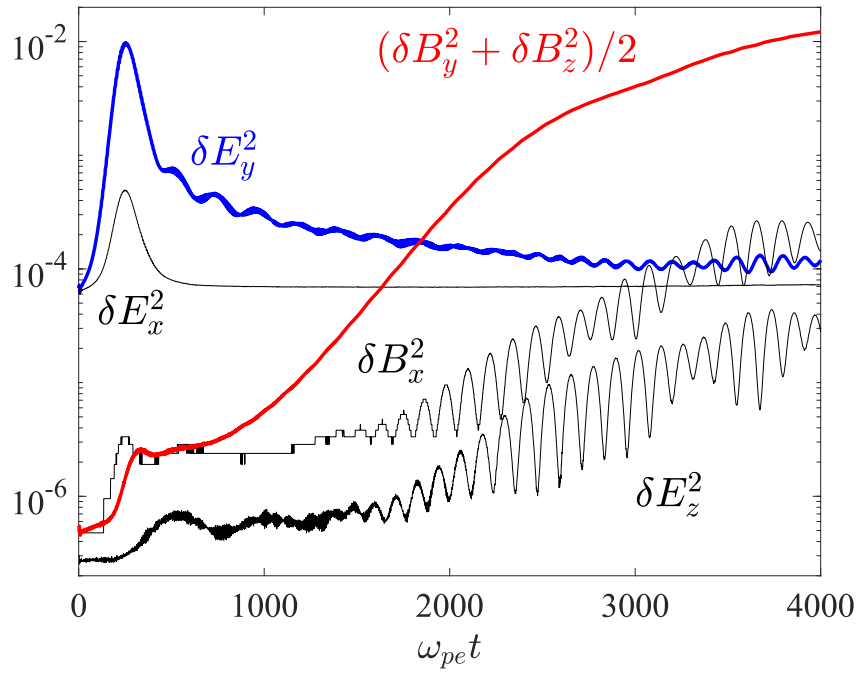

Figure 2. The result of 2D PIC simulation. The relatively early dynamics is dominated by the excitation of δE_y field, with a much weaker δE_x field excitation. The z component electric field is extremely low. The longer time-scale dynamics, however, is dictated by the y and z component magnetic wave fields, which are combined as $(\delta B_y^2 + \delta B_z^2)/2$. The x component wave magnetic field is also very low.

To see that indeed, the early excitation of predominantly y-component electric field (which implies quasi electrostatic—see Figure 1), δE_y, is associated with the quasi-perpendicular propagation, while the late excitation of $\delta B_\perp = (\delta B_y^2 + \delta B_z^2)/2$ is associated with the quasi-parallel mode, we plot the 2D spectra of the magnetic field energy density $\delta B_\perp$ and the electric field energy density δE_y in Figure 3. In the top left-hand panel of Figure 3, the 2D spectrum of frequency-integrated magnetic field, $\int d\omega |\delta B_\perp(k_\perp, k_\parallel, \omega)|^2$, where $\delta B_\perp^2 = (\delta B_y^2 + \delta B_z^2)/2$, is shown as a function of $ck_\perp/\omega_{pe}$ and $ck_\parallel/\omega_{pe}$. Likewise, on the top right-hand panel of Figure 3, the frequency-integrated electric field spectrum, $\int d\omega |\delta E_y(k_\perp, k_\parallel, \omega)|^2$, is plotted versus $ck_\perp/\omega_{pe}$ and $ck_\parallel/\omega_{pe}$. As is apparent, the magnetic field spectrum is indeed dominated by the quasi-parallel component, which also shows that the peak intensity takes place for $ck_\parallel/\omega_{pe} \sim 1$. That is, the quasi-parallel electromagnetic mode is of the long wavelength variety. Also apparent is the behavior associated with the quasi-perpendicular mode dominated by δE_y. This mode is characterized by the short wavelength, the characteristic $ck_\perp/\omega_{pe}$ having the value close to 10 or so. Underneath the top two panels depicting the frequency-integrated spectra, we also plot snapshots of 2D spectra for both $\delta B_\perp^2$ and δE_y^2 at selected time steps. Specifically, for the quasi-parallel mode, the bottom left-hand panel plots the 2D magnetic field spectrum at $\omega_{pe}t = 200$. In the left-hand panel just above, the same spectrum at $\omega_{pe}t = 1000$ is shown. And in the panel above that, we show the snapshot of $\delta B_\perp^2$ at $\omega_{pe}t = 3000$. One can see how the relatively low level of $\delta B_\perp^2(k_\perp, k_\parallel)$ gradually increases as time progresses. One can also discern that the evolution of instantaneous 2D spectrum is consistent with the frequency-integrated spectrum. We also plot the corresponding instantaneous electric field spectrum at selected time steps, but since the δE_y^2 field grows and saturates early, reaching peak intensity around $\omega_{pe}t \sim 200$ or so, and then subsequently undergoing reduction in wave intensity, we chose relatively early time steps, $\omega_{pe}t = 50$, 100 and 200. It is interesting to note that the peak intensity for δE_y^2 actually reaches its peak at $\omega_{pe}t = 100$ and that by the time the system evolves to $\omega_{pe}t = 200$, the peak intensity is slightly lower than that at $\omega_{pe}t = 100$. However, it should also be noted that at $\omega_{pe}t = 200$, the spectral broadening has taken place along $k_\perp$ direction. The cumulative 2D spectrum, which the frequency-integrated spectrum shown on the top-right panel corresponds to, collectively depicts the overall spectral behavior.

21699402, 2025, 2, Downloaded from https://agupubs.onlinelibrary.wiley.com/doi/10.1029/2024JA033285 by University Of Maryland, Wiley Online Library on [14/02/2025]. See the Terms and Conditions (https://onlinelibrary.wiley.com/terms-and-conditions) on Wiley Online Library for rules of use; OA articles are governed by the applicable Creative Commons License

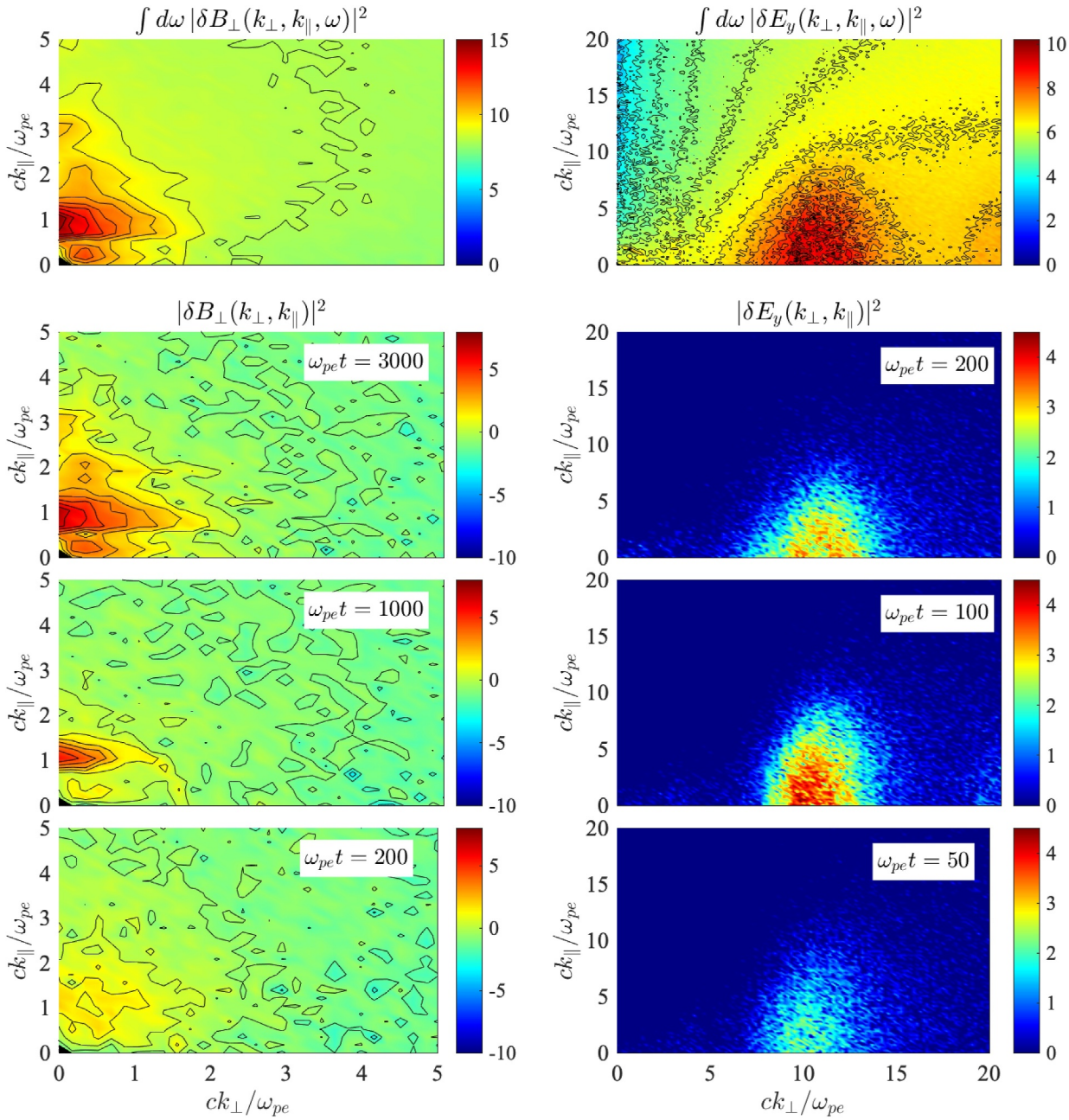

Figure 3. (Left-top) 2D spectrum of frequency-integrated magnetic field, $\int d\omega|\delta B_\perp(k_\perp, k_\parallel, \omega)|^2$, where $\delta B_\perp^2 = (\delta B_y^2 + \delta B_z^2)/2$. (Right-top) the frequency-integrated electric field spectrum, $\int d\omega|\delta E_y(k_\perp, k_\parallel, \omega)|^2$, versus $ck_\perp/\omega_{pe}$ and $ck_\parallel/\omega_{pe}$. Underneath the top two panels depicting the two spectra, we also plot the instantaneous 2D spectra taken at selected time steps, as indicated in the panels.

The quasi-parallel and quasi-perpendicular modes, respectively, can further be identified as the whistler and upper-hybrid modes. To confirm this, we carry out the temporal spectral transformation and generate the power spectral density (PSD), of PSD for short. In Figure 4 top left-hand panel, the PSD of $\delta B_\perp$ field is shown in $k_\parallel$-ω space. The temporal Fourier spectral transformation is taken over the time interval $200 < \omega_{pe}t < 3000$. On the top right, the PSD of δE_y field component is shown in $k_\perp$-ω space. For this component, the spectral transformation is taken over the time interval $0 < \omega_{pe}t < 200$. For later comparison against the quasilinear modeling, we also show in the bottom panels, the dynamic spectra for both the parallel and perpendicular modes. Specifically, on the bottom-left panel, we plot $\delta B_\perp$ spectrum against $ck_\parallel/\omega_{pe}$ and $\omega_{pe}t$. Likewise, we plot on the bottom-right, the

21699402, 2025, 2, Downloaded from https://agupubs.onlinelibrary.wiley.com/doi/10.1029/2024JA033285 by University Of Maryland, Wiley Online Library on [14/02/2025]. See the Terms and Conditions (https://onlinelibrary.wiley.com/terms-and-conditions) on Wiley Online Library for rules of use; OA articles are governed by the applicable Creative Commons License

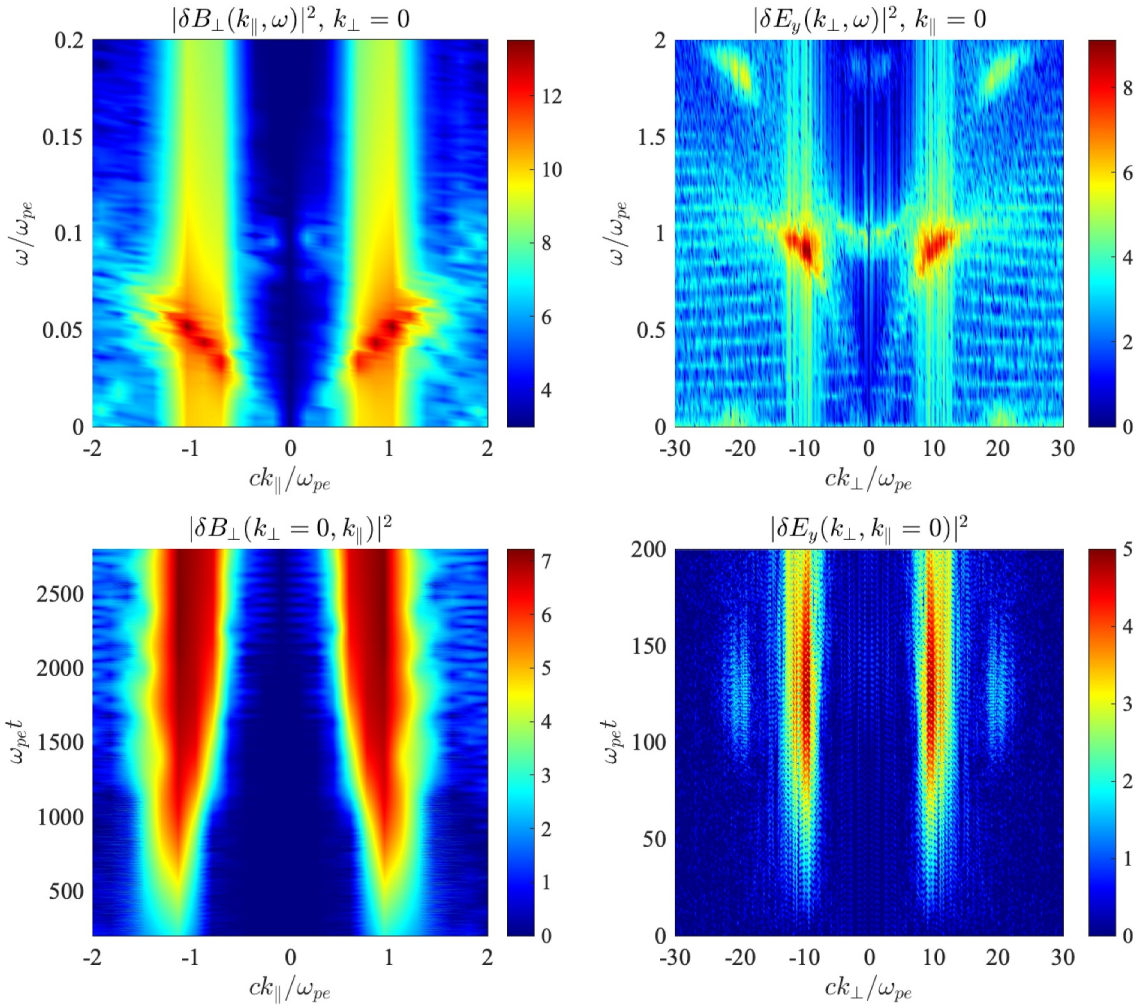

Figure 4. (Left-top) The power spectral density (PSD) of $\delta B_\perp$ field is shown in $k_\parallel$-ω space. The temporal Fourier spectral transformation is taken over the time interval $200 < \omega_{pe}t < 3000$. (Right-top) The PSD of δE_y field component is shown in $k_\perp$-ω space. For this component, the spectral transformation is taken over the time interval $0 < \omega_{pe}t < 200$. (Left-bottom) The dynamic spectrum for the quasi-parallel mode, that is, $\delta B_\perp$ spectrum versus $ck_\parallel/\omega_{pe}$ and $\omega_{pe}t$. [Right-bottom] The dynamic spectrum for quasi-perpendicular mode, namely, δE_y spectrum versus $ck_\parallel/\omega_{pe}$ and $\omega_{pe}t$.

electric field spectrum δE_y against $ck_\parallel/\omega_{pe}$ and $\omega_{pe}t$. The magnetic field PSD shows that the peak wave frequency takes place in the vicinity of $\omega \sim 0.05\omega_{pe} \sim 0.5\Omega_{ce}$, which along with the wavelength, $ck_\parallel/\omega_{pe} \sim 1$, clearly shows that this mode is indeed the whistler mode. Likewise, the PSD for the quasi-perpendicular mode clearly exhibits the peak fluctuation intensity in the close vicinity of the upper-hybrid frequency, $\omega \sim \omega_{uh} = \sqrt{\omega_{pe}^2 + \Omega_{ce}^2} \approx \omega_{pe}$ (for the present choice of input parameter $\omega_{pe}/\Omega_{ce} = 10$). It is noteworthy that the excitation of the dominant upper-hybrid mode fluctuation is accompanied by multiple-harmonic electron cyclotron, or Bernstein, modes. Another noteworthy fact is the excitation of weak harmonic component of the upper-hybrid mode with the property of twice the upper-hybrid frequency, $\omega \sim 2\omega_{uh} \sim 20$, and with one-half the perpendicular wavelength, $ck_\perp/\omega_{pe} \sim 20$. This appears to be the magnetized plasma analogue of the harmonic Langmuir wave, which is seen in the typical simulation of unmagnetized plasma (bump-in-tail) simulation (Gaelzer et al., 2003; Li et al., 2021; Umeda et al., 2003; Yoon et al., 2003), but as indicated by the dynamic spectrum, shown on the bottom-right panel, the harmonic upper-hybrid mode is a transient phenomenon, which peaks in its intensity, around $\omega_{pe}t \sim 125$, and subsequently subsides.

Next, we seek to explore the impact of instability excitation on the dynamics of the particles. In Figure 5, we thus plot the VDFs for the background electrons (black contours) and the ring electrons (red contours) at four

21699402, 2025, 2, Downloaded from https://agupubs.onlinelibrary.wiley.com/doi/10.1029/2024JA033285 by University Of Maryland, Wiley Online Library on [14/02/2025]. See the Terms and Conditions (https://onlinelibrary.wiley.com/terms-and-conditions) on Wiley Online Library for rules of use; OA articles are governed by the applicable Creative Commons License

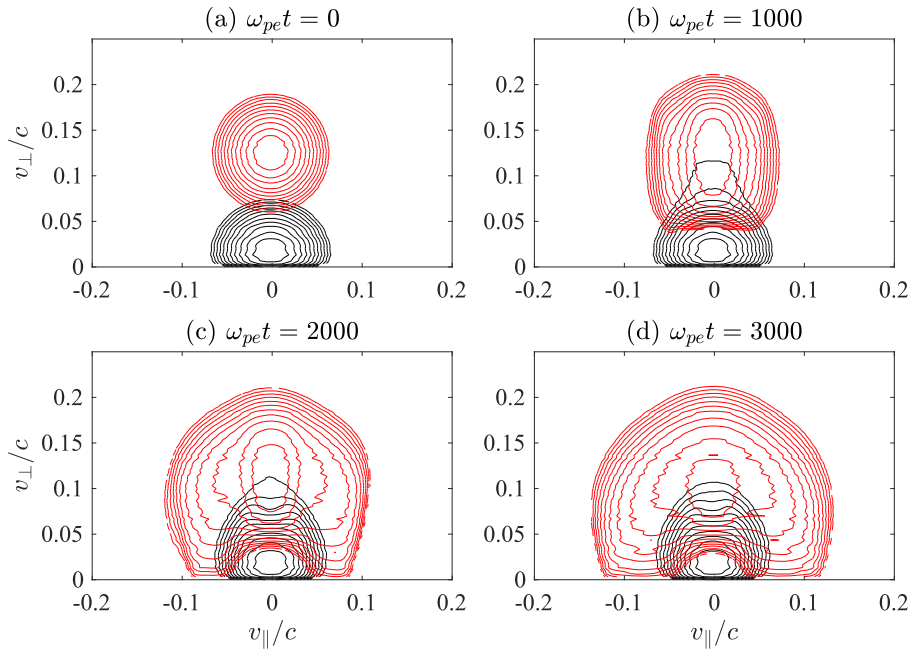

Figure 5. The electron velocity distributions are shown at four different times. The background and ring electrons are shown in black and red curves, respectively.

different time intervals. On panel (a), we plot the initial VDFs. As shown in Figure 2, the early excitation, saturation, followed by the reabsorption of the upper-hybrid mode all take place roughly within time period of $0 < \omega_{pe}t < 1000$. Consequently, we plot the snapshot of VDFs at $\omega_{pe}t = 1000$ in panel (b). From this panel, we may discern the impact of the upper-hybrid mode excitation as having the consequence of a slight reduction of the ring speed, accompanied by a perpendicular thermal velocity spreading, while the background core electrons are slightly heated in the perpendicular direction. In the meantime, however, the parallel thermal spread apparently did not take place. As it will be shown with the subsequent quasilinear analysis, this is consistent with the theoretical prediction that the upper-hybrid does not influence the parallel temperature. The early-time dynamics of the present 2D simulation is reminiscent of the earlier 2D simulation by Umeda et al. (2007), the more recent 1D simulations by Lee et al. (2018) and Yoon and Omura (2023).

Also as can be seen from Figure 2, the subsequent long-term dynamics of the system is dominated by the slowly-growing whistler mode waves. From Figure 5 panels (c) and (d), the effects of the quasi-parallel electromagnetic whistler mode waves is to cause the electrons to diffuse in pitch-angle space, with the end result of the initial ring distribution slowly evolving into a partial shell distribution. The background electrons, which had undergone a slight perpendicular heating during the earlier phase of the upper-hybrid instability, have now also undergone the pitch-angle diffusion such that by the time system evolved to $\omega_{pe}t = 3000$, the background VDF has been smoothed out into a quasi isotropic form. The formation of partial shell VDF by the ring-driven whistler instability has been discussed by Yoon et al. (2019), where the authors carried out a 1D PIC simulation coupled with the quasilinear analysis. The present 2D simulation is qualitatively similar to their work albeit the present work is more general in that we encompass the two-dimensional dynamics.

While the separate contour plots of background and the initially ring electron populations as shown in Figure 5 is a useful construct, it is the combined distribution that controls the growth and damping of the waves. As such, it is informative to plot the combined VDF at the same time intervals shown in Figure 5. We thus display this result in Figure 6. From this, it can be seen that at $\omega_{pe}t = 1000$ the ring component has undergone a perpendicular velocity spread while the parallel temperature remains unchanged. The configuration is equivalent to the velocity plateau formation along perpendicular direction, highly reminiscent of the well-known saturation stage of the one-dimensional bump-on-tail Langmuir wave instability (Davidson, 1972; Sagdeev & Galeev, 1969). As may be gleaned from Figures 6c and 6d, the excitation of quasi-parallel transverse whistler-mode instability leads to the

21699402, 2025, 2, Downloaded from https://agupubs.onlinelibrary.wiley.com/doi/10.1029/2024JA033285 by University Of Maryland, Wiley Online Library on [14/02/2025]. See the Terms and Conditions (https://onlinelibrary.wiley.com/terms-and-conditions) on Wiley Online Library for rules of use; OA articles are governed by the applicable Creative Commons License

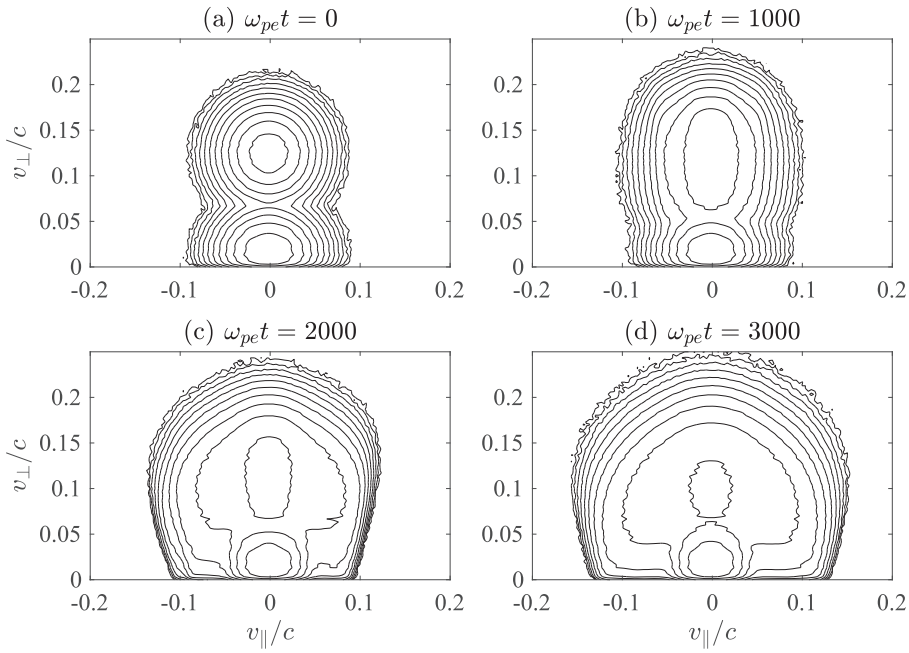

Figure 6. The combined (background plus energetic) electron velocity distributions are shown at the same four different times shown in Figure 6.

gradual pitch-angle scattering, which leads to the formation of the partial shell distribution during the time period corresponding to $2000 < \omega_{pe}t < 3000$.

4. Interpretation of 2D PIC Simulation With Quasilinear Theory

4.1. Modeling Early Time Evolution By Upper-Hybrid/Bernstein Mode Instability Excitation and Saturation

To recap the findings based on the 2D PIC simulation, it shows that early on, quasi-perpendicular, quasi-electrostatic upper-hybrid mode instability is excited, accompanied by excitation of multiple-harmonic electron cyclotron (Bernstein) modes. The predominantly quasi-electrostatic upper-hybrid mode leads to the reduction of the perpendicular ring speed as well as an increase of the thermal spread along the perpendicular direction. Again to recap, this is very similar to the 1D electrostatic simulation, first carried out by Lee et al. (2018), and analyzed in more detail by Yoon and Omura (2023). Over longer time interval, on the other hand, the thermal ring distribution begins to spread in pitch angle space, forming a partial velocity shell distribution. Such a feature that takes place over a longer time period may be modeled by a partial shell velocity distribution, which was analyzed by Yoon et al. (2019). Even though these findings and interpretations are already available, it is worthwhile to compile these results in the present paper to provide a comprehensive overview of the present state of knowledge. For this reason, we will revisit the interpretation of the 2D PIC simuation in light of the quasilinear theory. We make note of the fact that during the relatively early phase, the process can be quite accurately described by a perpendicular ring VDF with increasing perpendicular thermal spread and a slight reduction of ring speed, while the parallel thermal spread remains unchanged—see the time evolution between $\omega_{pe}t = 0$ and 1,000 in Figures 2 and 5. Moreover, we may simplify the analysis by assuming that only the electrostatic mode grows and saturates during this time period. With this assumption, we first discuss the thermal ring-driven Bernstein mode instability problem, which was recently developed by Yoon and Omura (2023), which in turn, improved the earlier theory by Lee et al. (2018).

To recapitulate their theory (Yoon & Omura, 2023), the ring model to be used for initial growth rate calculation as well as for quasilinear velocity moment calculation is given by

21699402, 2025, 2, Downloaded from https://agupubs.onlinelibrary.wiley.com/doi/10.1029/2024JA033285 by University Of Maryland, Wiley Online Library on [14/02/2025]. See the Terms and Conditions (https://onlinelibrary.wiley.com/terms-and-conditions) on Wiley Online Library for rules of use; OA articles are governed by the applicable Creative Commons License

$$f_r(v_\perp, v_\parallel) = \frac{n_r/n_0}{\pi^{3/2}A_1\alpha_\perp^2\alpha_\parallel}\exp\left(-\frac{(v_\perp - V_r)^2}{\alpha_\perp^2} - \frac{v_\parallel^2}{\alpha_\parallel^2}\right),$$
$$A_1 = 2\int_0^\infty dx x \exp\left[-\left(x - \frac{V_r}{\alpha_\perp}\right)^2\right], \quad (1)$$
$$\alpha_\perp^2 = \frac{2T_\perp}{m_e}, \qquad \alpha_\parallel^2 = \frac{2T_\parallel}{m_e}.$$

Here, $\alpha_\perp$ and $\alpha_\parallel$ denote the thermal speeds associated with the ring electron distribution function along perpendicular and parallel directions, respectively. The perpendicular and parallel "temperatures," $T_\perp$ and $T_\parallel$, are defined via their respectively thermal speeds, $\alpha_\perp$ and $\alpha_\parallel$. The perpendicular ring speed is given by V_r. The number density of the ring component is n_r, while the total (background plus ring) electron number density is given by n_0. The background ("cold") is considered to be given by an isotropic Maxwellian distribution for all time,

$$f_c(v) = \left(1 - \frac{n_r}{n_0}\right)\frac{1}{\pi^{3/2}\alpha_c^3}\exp\left(-\frac{v^2}{\alpha_c^2}\right), \qquad \alpha_c^2 = \frac{2T_c}{m_e}. \quad (2)$$

Here, α_c is the background thermal speed, and T_c represents the background electron temperature. Note that the simulation shows that the background electrons undergo a slight perpendicular heating (Figure 5). However, the degree of heating is quite low and it seems to have relatively little impact on an overall sense. We thus assume that the background remains constant. In the present analysis, the temperature is defined in terms of thermal energy (eV) so that the Boltzmann constant is absent in the definition for thermal speed. In the simulation the initial input parameters are $\alpha_\perp/c = \alpha_\parallel/c = 0.025 = \alpha_c/c$ and $V_r/\alpha_\perp = 5$. The normalization constant A_1 can be obtained in closed form as $A_1 = \exp\left(-V_r^2/\alpha_\perp^2\right) + (V_r/\alpha_\perp)\sqrt{\pi}[1 + \mathrm{erf}(V_r/\alpha_\perp)]$. However, we choose to compute the x integral numerically. This is because, in the quasilinear velocity moment calculation, we will encounter other x integrals of the form,

$$A_n = 2\int_0^\infty dx x^n \exp\left[-\left(x - \frac{V_r}{\alpha_\perp}\right)^2\right], \quad (3)$$

for which analytical closed-form manipulations become cumbersome, so that it is much more straightforward to compute these integrals numerically. For the sake of consistency, we therefore, choose to compute the normalization constant A_1 numerically as well.

The dominant thermal background electrons comprise 90% of the density. These background electrons (denoted by c—meaning either "cold" or "core") support the waves. During the early phase of the simulation, the waves are predominantly quasi-perpendicular electrostatic in nature, whose dispersion relation is given by

$$0 = \epsilon(k_\perp, \omega) = 1 + \frac{2\omega_{pe}^2}{k_\perp^2\alpha_c^2}\left(1 - \sum_{n=-\infty}^{\infty} I_n(\lambda)\, e^{-\lambda}\, \frac{\omega}{\omega - n\Omega_e}\right), \qquad \lambda = \frac{k_\perp^2\alpha_c^2}{2\Omega_e^2}. \quad (4)$$

in Equation 4, the quantity $I_n(x)$ is the modified Bessel function of the first kind of order n. To determine the instability, we retain relativistic effects since without the relativistic correction, there is no wave-particle resonance for exactly 90° propagation—see, for example, (Umeda et al., 2007), who adopted the non-relativistic formalism and demonstrate that the upper-hybrid mode excitation occurs for oblique angles of propagation, but not at exactly perpendicular propagation angle. The specific form for the growth/damping rate is thus given by

$$\omega_i = \frac{\pi}{R}\frac{4\pi n_0 e^2}{k_\perp^2}\int d\mathbf{p}\sum_{n=-\infty}^{\infty} J_n^2\left(\frac{k_\perp v_\perp \gamma}{\Omega_e}\right)\delta\left(\omega_r - \frac{n\Omega_e}{\gamma}\right)\frac{\omega_r}{v_\perp}\frac{\partial f_r(\mathbf{p})}{\partial p_\perp},$$
$$R = \sum_{n=1}^{\infty}\frac{4n^2\Lambda_n(\lambda)}{\lambda}\frac{\omega_r\omega_{pe}^2}{\left(\omega_r^2 - n^2\Omega_e^2\right)^2}. \quad (5)$$

21699402, 2025, 2, Downloaded from https://agupubs.onlinelibrary.wiley.com/doi/10.1029/2024JA033285 by University Of Maryland, Wiley Online Library on [14/02/2025]. See the Terms and Conditions (https://onlinelibrary.wiley.com/terms-and-conditions) on Wiley Online Library for rules of use; OA articles are governed by the applicable Creative Commons License

Here, ω_r is the real frequency, which is determined from the dispersion relation (Equation 4) and f_r is the ring electron distribution function (Equation 1). In Equation 5, the quantity $J_n(x)$ is the Bessel function of the first kind of order n. In the weakly relativistic approach the above expression is approximated by approximating all relativistic mass factor γ by unity, except in the resonance condition, where it is approximated by $\gamma \approx 1 + v^2/2c^2$. We can also replace the momentum representation to velocity representation by making use of $f_r(\mathbf{p})\, d\mathbf{p} = f_r(\mathbf{v})\, d\mathbf{v}$. Implementing all this, Yoon and Omura (2023) show that for the ring distribution, the growth rate for positive n is given by

$$\begin{aligned}
\omega_i &= -\frac{n_r}{n_0}\frac{8\pi^{1/2}}{A_1 R}\frac{\omega_{pe}^2}{k_\perp^2}\frac{c^2}{\alpha_\perp^3\alpha_\parallel}\sum_{n=1}^{\infty}\Theta\left(n\Omega_e-\omega_r\right)\int_0^{x_*} dx\, Q_n(x) \equiv \sum_{n=1}^{\infty}\omega_i^n,\\
Q_n(x) &= \frac{1}{\sqrt{x_*^2-x^2}}\left(x-\frac{V_r}{\alpha_\perp}\right)J_n^2\left(\frac{k_\perp\alpha_\perp}{\Omega_e}x\right)\exp\left[-\left(x-\frac{V_r}{\alpha_\perp}\right)^2-\frac{\alpha_\perp^2}{\alpha_\parallel^2}\left(x_*^2-x^2\right)\right],\\
x_*^2 &= \frac{2c^2}{\alpha_\perp^2}\frac{n\Omega_e-\omega_r}{\omega_r}.
\end{aligned} \tag{6}$$

In the above, we have expressed the total growth rate ω_i as a sum of individual growth rates for each harmonic mode, ω_i^n.

Next, we consider the electrostatic quasilinear theory, which will be employed to model the early-time evolution of the initial ring electron velocity distribution. The basic methodology is already discussed in Yoon and Omura (2023)—see also, the earlier work by Lee et al. (2018), but herewith we briefly overview the formalism for the sake of completeness. The quasilinear particle kinetic equation in the weakly relativistic approximation, and for electrostatic wave modes propagating in perpendicular direction with respect to the ambient magnetic field, is given by

$$\begin{aligned}
\frac{\partial f_r}{\partial t} &= \frac{2\pi^2 e^2}{m_e^2}\sum_n\int_0^{\infty}\frac{dk_\perp k_\perp}{\omega_r}\frac{n\Omega_e}{v_\perp}\frac{\partial}{\partial v_\perp}\\
&\quad\times J_n^2\left(\frac{k_\perp v_\perp}{\Omega_e}\right)W(k_\perp)\,\delta\left(\frac{v^2}{2c^2}-\frac{n\Omega_e-\omega_r}{\omega_r}\right)\frac{n\Omega_e}{v_\perp}\frac{\partial f_r}{\partial v_\perp},
\end{aligned} \tag{7}$$

where $W(k_\perp) = \langle\phi^2(k_\perp)\rangle$ is the spectral wave energy density associated with the electrostatic upper-hybrid/Bernstein modes. Note that $W(k_\perp)$ is the summation of all the harmonic modes, $W(k_\perp) = \sum_n W_n(k_\perp)$, with each sub intensity satisfying the wave kinetic equation $\partial W_n(k_\perp)/\partial t = 2\omega_i^n(k_\perp)\, W_n(k_\perp)$. In Equation 7, ω_r is obtained from the instantaneous dispersion relation (Equation 4). The 2D PIC simulation shows that the early-time evolution may be modeled by the ring model, except that the ring speed and perpendicular thermal spread evolve separately. The same property was also observed in the 1D ES PIC simulation (Yoon & Omura, 2023). We thus allow V_r and $\alpha_\perp$ to be functions of time. The dynamical equations for these quantities can be obtained upon taking the velocity moments of the quasilinear kinetic Equation 7,

$$\begin{aligned}
\frac{\partial}{\partial t}\int d\mathbf{v}\, v_\perp^l f_r &= -l\,\frac{4\pi^3 e^2}{m_e^2}\sum_n n^2\Omega_e^2\int_0^{\infty}\frac{dk_\perp k_\perp}{\omega_r}\int_{-\infty}^{\infty}dv_\parallel\int_0^{\infty}dv_\perp v_\perp^{l-2}\\
&\quad\times J_n^2\left(\frac{k_\perp v_\perp}{\Omega_e}\right)W(k_\perp)\,\delta\left(\frac{v_\perp^2}{2c^2}+\frac{v_\parallel^2}{2c^2}-\frac{n\Omega_e-\omega_r}{\omega_r}\right)\frac{\partial f_r}{\partial v_\perp},
\end{aligned} \tag{8}$$

where $l = 0, 1, 2, \ldots$.

Yoon and Omura (2023) shows that the evolution equations for V_r and $\alpha_\perp$ can be obtained on the basis of velocity moment equations corresponding to $l = 1$ and 2. Yoon and Omura (2023) also discussed that $\alpha_\parallel$ remains constant, both according the quasilinear theoretical prediction and in the 1D ES PIC code simulation. The resulting dynamical equations for V_r and $\alpha_\perp$ are shown below,

21699402, 2025, 2, Downloaded from https://agupubs.onlinelibrary.wiley.com/doi/10.1029/2024JA033285 by University Of Maryland, Wiley Online Library on [14/02/2025]. See the Terms and Conditions (https://onlinelibrary.wiley.com/terms-and-conditions) on Wiley Online Library for rules of use; OA articles are governed by the applicable Creative Commons License

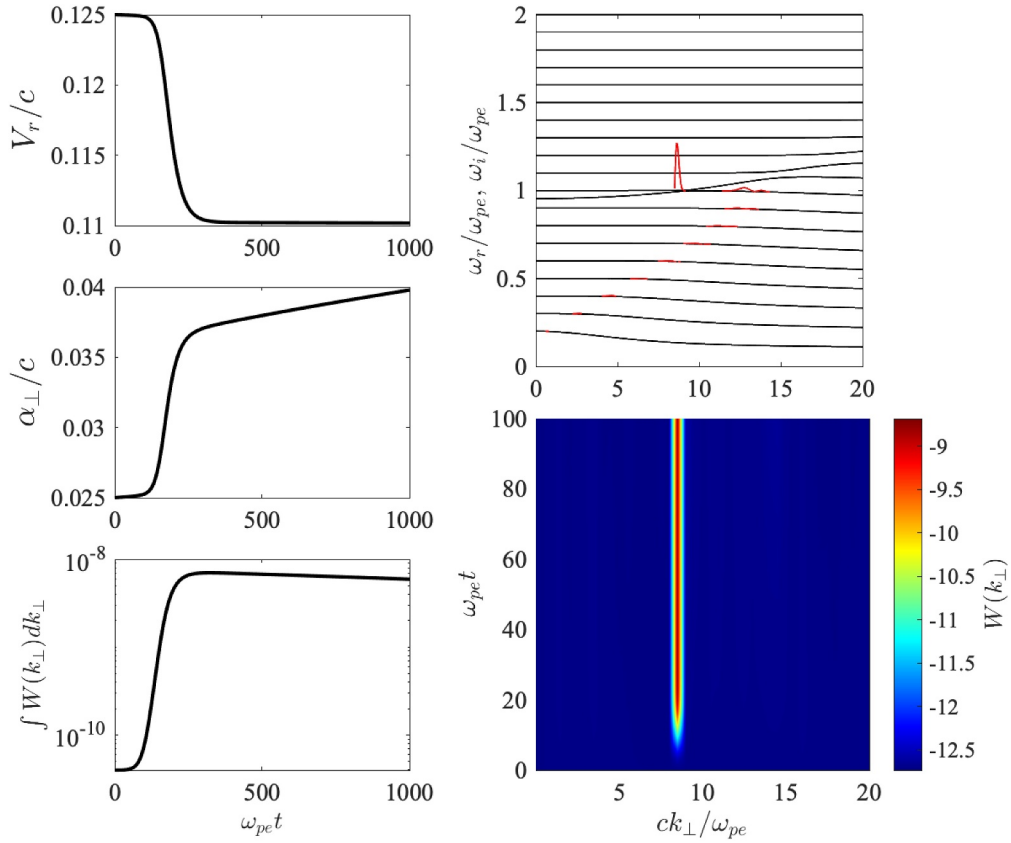

Figure 7. Numerical solution of Equation 9, together with the solution of the wave kinetic equation. The left-hand panels show, from top, the time evolution of normalized perpendicular ring speed, V_r/c, perpendicular thermal spread, $\alpha_\perp/c$, and the integrated electrostatic wave energy density, $\int dk_\perp W(k_\perp)$, versus normalized time, $\omega_{pe}t$. The right-hand panels show the initial linear dispersion relation and the associated growth rate (top panel) and the dynamic spectrum (bottom panel).

$$\frac{dV_r}{dt} = -\frac{c_{21}S_1 - c_{11}S_2}{D}, \qquad \frac{d\alpha_\perp}{dt} = \frac{c_{22}S_1 - c_{12}S_2}{D}, \qquad D = c_{11}c_{22} - c_{12}c_{21},$$
$$c_{11} = \frac{A_2}{A_1} - c_{12}\,\frac{V_r}{\alpha_\perp}, \qquad c_{12} = \frac{2\left(A_1A_3 - A_2^2\right)}{A_1^2},$$
$$c_{21} = 2\alpha_\perp\,\frac{A_3}{A_1} - c_{22}\,\frac{V_r}{\alpha_\perp}, \qquad c_{22} = 2\alpha_\perp\,\frac{A_1A_4 - A_2A_3}{A_1^2}, \tag{9}$$
$$S_1 = \frac{n_r}{n_0}\frac{16\pi^{3/2}e^2}{m_e^2A_1}\frac{c^2}{\alpha_\perp^4\alpha_\parallel}\int_0^\infty dk_\perp k_\perp \sum_{n=1}^\infty \Theta(n\Omega_e - \omega_r)\,\frac{n^2\Omega_e^2}{\omega_r}\,W(k_\perp)\int_0^{x_*} dx\,\frac{Q_n(x)}{x},$$
$$S_2 = \frac{n_r}{n_0}\frac{32\pi^{3/2}e^2}{m_e^2A_1}\frac{c^2}{\alpha_\perp^3\alpha_\parallel}\int_0^\infty dk_\perp k_\perp \sum_{n=1}^\infty \Theta(n\Omega_e - \omega_r)\,\omega_r W(k_\perp)\int_0^{x_*} dx\,Q_n(x),$$

where the quantity $Q_n(x)$is already defined in Equation 6, and the coefficient A_n was introduced in Equation 3.

Numerical solution of the set of Equation 9, together with the solution of the wave kinetic equation, is shown in Figure 7. The plot of numerical roots of the dispersion relation (Equation 4) and the associated growth rate for each harmonic mode is shown on the upper-right panel. The growth rate is plotted atop the real frequency by shifting the growth rate along vertical axis by adding the corresponding real frequency to the value of the growth rate. The black curves denote the real frequency, while the red curves depict the growth rate. That is, the plotted quantities are $(\omega_i + n)/\omega_{pe}$, where n corresponds to the integer value of normalized frequency, int(ω_r/Ω_e). The cumulative multiple-harmonic Bernstein modes display the upper-hybrid wave characteristics (the dispersive

21699402, 2025, 2, Downloaded from https://agupubs.onlinelibrary.wiley.com/doi/10.1029/2024JA033285 by University Of Maryland, Wiley Online Library on [14/02/2025]. See the Terms and Conditions (https://onlinelibrary.wiley.com/terms-and-conditions) on Wiley Online Library for rules of use; OA articles are governed by the applicable Creative Commons License

21699402, 2025, 2, Downloaded from https://agupubs.onlinelibrary.wiley.com/doi/10.1029/2024JA033285 by University Of Maryland, Wiley Online Library on [14/02/2025]. See the Terms and Conditions (https://onlinelibrary.wiley.com/terms-and-conditions) on Wiley Online Library for rules of use; OA articles are governed by the applicable Creative Commons License

property) starting from the upper-hybrid frequency $\omega_{UH} = \sqrt{\omega_{pe}^2 + \Omega_e^2} = \sqrt{101}\Omega_e \sim 10\Omega_e$ (or $\omega_r/\omega_{pe} \sim 1$), which connects to progressively higher harmonics. The growth rate superposed on top of real frequency, shows that the most unstable mode takes place around the upper-hybrid frequency, and the most unstable perpendicular wave number is slightly below $ck_\perp/\omega_{pe} \sim 10$, which is consistent with the simulation result. For the details of Figure 7, see the caption thereof. The reduction of the perpendicular ring speed (top-left) and concomitant increase of perpendicular thermal spread (middle-left) are consistent with the analysis carried out by Yoon and Omura (2023), and is also consistent with the present 2D PIC simulation. The dynamic spectrum is shown on the lower right panel. Upon comparison with the PIC simulation result, shown in Figure 4, it can be seen that the overall range of perpendicular wave numbers over which the spectrum is enhanced is qualitatively similar. However, one may also notice that the peak $k_\perp$ is slightly reduced in the case of quasilinear theory, and moreover, the width of the spectrum is wider in the case of PIC simulation. Despite these, it is also quite obvious that there exists a reasonable convergence between the theory and simulation. The bottom-left panel plots the evolution of electrostatic wave intensity in time. This roughly corresponds to the δE_y component in Figure 2. It can be seen judging from the dynamic spectrum [bottom-right] that the most unstable mode predicted by the initial linear dispersive property in Figure 7, shown on the top-right panel, remains the only prominent unstable mode throughout the entire time evolution. Again, this is similar to the findings by Yoon and Omura (2023), and also consistent with the 2D PIC simulation result in that, the most unstable quasi-perpendicular mode in the 2D simulation takes place for $ck_\perp/\omega_{pe}$ slightly below 10, with the frequency in the close vicinity of the upper-hybrid frequency—see Figure 4. The time scale of instability excitation and saturation (around $\omega_{pe}t \sim 200$) is also consistent with the 2D simulation result—see Figure 2. However, we also see a notable difference. Specifically, the simulation result in Figure 2 shows the initial exponential increase of electrostatic wave energy density, which reaches a peak intensity, but the subsequent dynamics shows gradual decrease in the wave energy density. In contrast, the quasilinear calculation of electrostatic wave energy density does not show much long-term decrease in the wave energy density, although the initial exponential increase and subsequent saturation behavior, especially in terms of the time scale, are in an overall agreement. Such a discrepancy could be the result of restricting the calculation to exactly-perpendicular propagation, or it could be related to the electrostatic approximation. Also, in the quasilinear calculation we held the background core electron temperature to be constant, whereas in reality, the core (or cold) electrons are heated in the perpendicular direction by the instability excitation, thus contributing to the reabsorption of the wave energy density. Despite these small discrepancies, the overall good agreement between the quasilinear theory and the early stage of the simulation shows that the 2D PIC simulation can be interpreted in the light of early phase of upper-hybrid mode excitation and saturation.

To further confirm this, we reconstruct the electron VDF at $\omega_{pe}t = 1000$ based on the velocity moments, V_r/c and $\alpha_\perp/c$, computed from the quasilinear theory, and plot the result next to the initial VDF. The result is shown in Figure 8, where we plot the velocity distribution, $2\pi v_\perp f_r(v_\perp, v_\parallel)$. Specifically, the top two panels separately plot the contours of the ring (red) versus background (black) electron populations, and the bottom two panels show the combined (or total) electron distribution at two different times, $\omega_{pe}t = 0$ and 1,000. This result can be compared against the 2D PIC simulation result shown in the upper two panels of Figure 5 or those of Figure 6. As one may appreciate, the comparison is quite reasonable.

4.2. Modeling Long Time Evolution by Whistler Mode Instability Excitation

Over the longer time scale, up to $\omega_{pe}t = 3000$, the 2D EM PIC simulation shows that the whistler mode instability is dynamically more important. While the early phase of the simulation is dominated by the excitation of upper-hybrid mode instability excitation, the electrostatic mode eventually decreases in magnitude. The effects of the electrostatic upper-hybrid mode excitation is to decrease the perpendicular ring velocity somewhat and to increase the perpendicular velocity spread accordingly. As discussed in the previous sub-section, these behaviors were adequately described by employing a 1D ES quasilinear theory of upper-hybrid instability. However, after the ES upper-hybrid instability saturation, a substantial degree of perpendicular effective temperature anisotropy remains, which is unstable to the whistler mode (or EM electron cyclotron—EMEC for short) instability. The simulation shows that the excitation of whistler instability leads to the pitch-angle diffusion, which causes the VDF to evolved into the partial velocity shell distribution. The formation of such a partial shell distribution from the initial ring distribution was already addressed in a study by Yoon et al. (2019), but in that work, we employed a 1D EM PIC simulation combined with 1D quasilinear analysis with the assumption of dynamical processes taking

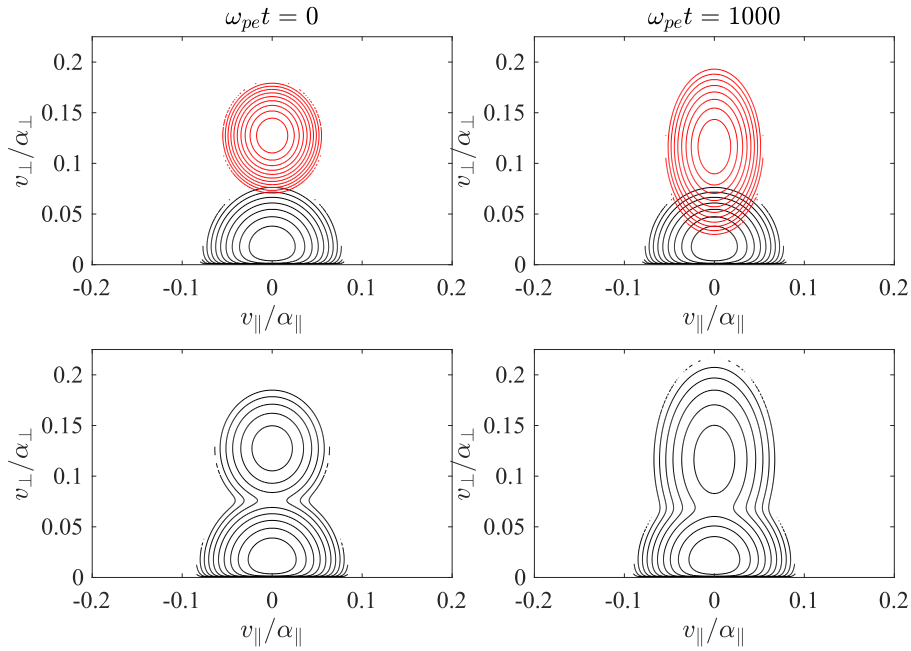

Figure 8. The electron velocity distribution function, $2\pi v_\perp f_r\left(v_\perp, v_\parallel\right)$, at initial time $t = 0$ (top and bottom left) and at $\omega_{pe}t = 1000$ [top and bottom right], where the distribution function is reconstructed based on the velocity moments, V_r/c and $\alpha_\perp/c$ computed from the quasilinear theory. Top two panels separately plot the contours of ring and background populations, while the bottom two panels show the combined distribution at two different times.

place along the direction of ambient magnetic field. Here, we repeat the quasilinear analysis for the sake of completeness, and with the purpose of interpreting the present 2D simulation. As the basic underlying theoretical development can be found in our previous paper (Yoon et al., 2019), the theoretical formulation will be a brief survey but nevertheless with sufficient details.

In the simulation and in the quasilinear theory electrostatic upper-hybrid instability we made use of the ring electron distribution (Equation 1). However, unlike the previous discussion on the upper-hybrid mode excitation, the subsequent time evolution of the "hot" electron VDF can no longer be described by the perpendicular ring model as the subsequent dynamics of pitch-angle diffusion turns the initial ring model into a partial shell model. Thus, in the theoretical model of the quasi-linear development of the instability, we adopt the partial shell distribution,

$$\begin{aligned} f_{\rm shell} &= \frac{n_h}{n_0}\frac{1}{\pi^{3/2}\alpha^3\Delta{\rm erf}(1/\Delta)A_{\rm shell}}\exp\left(-\frac{(v-v_0)^2}{\alpha^2}-\frac{\mu^2}{\Delta^2}\right), \\ A_{\rm shell} &= ue^{-u^2}+\pi^{\frac{1}{2}}\left(\frac{1}{2}+u^2\right)[1+{\rm erf}(u)]. \end{aligned} \tag{10}$$

In the velocity moment-based quasilinear analysis, following the earlier approach by Yoon et al. (2019), we assume that only the parameter Δ evolves in time. This parameter controls the degree of isotropy in pitch angle space, thus, when $\Delta \to \infty$, the velocity distribution is a complete shell. In the work by Yoon et al. (2019), they discuss replacing the initial perpendicular ring velocity distribution by the partial shell model. This is done by comparing the effective perpendicular and parallel temperatures associated with both the thermal ring and partial shell distributions, and by choosing appropriate input parameters for the shell model in accordance with the corresponding ring model. By following the same procedures, we thus determine that for the input parameters of $\alpha/c = 0.025$ and $V_0/c = 0.125$, which is consistent with the initial conditions adopted in the 2D PIC simulation, we find that the choice of

$$\Delta = 0.1925 \tag{11}$$

21699402, 2025, 2, Downloaded from https://agupubs.onlinelibrary.wiley.com/doi/10.1029/2024JA033285 by University Of Maryland, Wiley Online Library on [14/02/2025]. See the Terms and Conditions (https://onlinelibrary.wiley.com/terms-and-conditions) on Wiley Online Library for rules of use; OA articles are governed by the applicable Creative Commons License

is a good representation of the initial ring VDF.

For the subsequent quasilinear analysis, we assume that all the dynamic processes take place in directions parallel and anti-parallel to the ambient magnetic field. We consider the real frequency for whistler mode propagating in parallel direction, whose dispersion relation is

$$\frac{\omega_r}{\Omega_e} = \frac{c^2 k_\parallel^2}{\omega_{pe}^2 + c^2 k_\parallel^2}. \tag{12}$$

The corresponding wave growth/damping rate is given by

$$\omega_i = \frac{\pi}{2}\frac{(\Omega_e - \omega_r)^2}{\Omega_e}\int d\mathbf{v}\, v_\perp \delta(\omega_r - k_\parallel v_\parallel - \Omega_e)\left(\Omega_e \frac{\partial f_{\rm shell}}{\partial v_\perp} + k_\parallel v_\perp \frac{\partial f_{\rm shell}}{\partial v_\parallel}\right). \tag{13}$$

As the parallel whistler-mode instability does not require relativistic wave-particle resonance condition, we hereby employ non-relativistic formalism. Upon inserting the partial shell VDF (10) we have—see (Yoon et al., 2019) for detail

$$\begin{aligned}
\omega_i &= -\pi^{1/2}\frac{n_h}{n_0}\frac{(\Omega_e - \omega_r)^4}{k_\parallel^2 |k_\parallel| \alpha^3}\frac{2}{A}\int_0^\infty dy\,\left[(y+1)^2 - 1\right] \\
&\times\left[\frac{\omega_r(\Omega_e - \omega_r)}{\Omega_e k_\parallel \alpha}\left(\frac{(\Omega_e - \omega_r)(y+1)}{k_\parallel \alpha} - u\right) + \frac{\omega_r}{\Omega_e}\frac{\eta^2\left[(y+1)^2 - 1\right]}{(y+1)^3} - \frac{\eta^2}{y+1}\right] \\
&\times \exp\left[-\left(\frac{(\Omega_e - \omega_r)(y+1)}{k_\parallel \alpha} - u\right)^2 - \frac{\eta^2}{(y+1)^2}\right], \\
A &= \frac{\mathrm{erf}(\eta)}{\eta}\left[u e^{-u^2} + \pi^{\frac{1}{2}}\left(\frac{1}{2} + u^2\right)\left[1 + \mathrm{erf}(u)\right]\right], \qquad u = \frac{v_0}{\alpha}, \qquad \eta = \frac{1}{\Delta}.
\end{aligned} \tag{14}$$

To discuss the quasi-linear development of the instability, we develop a dynamical theory of wave and particle kinetic theory. The wave kinetic equation follows the standard form. If we consider the transverse electric field energy density, δE^2, then the wave kinetic equation is $\partial \delta E^2/\partial t = 2\omega_i \delta E^2$. The magnetic field energy density, δB^2, is given by $\delta B^2 = \left[\left(\omega_p^2 + c^2 k_\parallel^2\right)^2 / \left(\Omega_e^2 c^2 k_\parallel^2\right)\right]\delta E^2$. The particle kinetic equation for the shell electron distribution function is

$$\begin{aligned}
\frac{\partial f_{\rm shell}}{\partial t} &= \frac{\pi e^2}{m_e^2}\int_{-\infty}^{\infty} dk_\parallel \frac{1}{v}\left(\frac{\partial}{\partial v} - \frac{\omega_r \mu - k_\parallel v}{v\omega_r}\frac{\partial}{\partial \mu}\right) v\left(1 - \mu^2\right) \\
&\times \delta E^2\left(k_\parallel\right)\delta\left(\omega_r - \Omega_e - k_\parallel v\mu\right)\left(\frac{\partial}{\partial v} - \frac{\omega_r \mu - k_\parallel v}{v\omega_r}\frac{\partial}{\partial \mu}\right) f_{\rm shell}.
\end{aligned} \tag{15}$$

Following our early work (Yoon et al., 2019), we assume that only Δ evolves in time. The velocity moment of interest to us is

$$\begin{aligned}
\frac{d}{dt}\int d\mathbf{v}\,\mu^2 f_{\rm shell} &= \frac{2\pi^2 e^2}{m_e^2}\int_{-\infty}^{\infty} dk_\parallel \int_{-1}^{1} d\mu\,\mu\left(1 - \mu^2\right)\int_0^\infty dv v\,\frac{3\omega_r \mu - 2k_\parallel v}{\omega_r} \\
&\times \delta E^2\left(k_\parallel\right)\delta\left(\omega_r - \Omega_e - k_\parallel v\mu\right)\left(\frac{\partial}{\partial v} - \frac{\omega_r \mu - k_\parallel v}{v\omega_r}\frac{\partial}{\partial \mu}\right) f_{\rm shell}.
\end{aligned} \tag{16}$$

Making use of this velocity moment, Yoon et al. (2019) derived the evolution equation for Δ, which is reproduced below:

21699402, 2025, 2, Downloaded from https://agupubs.onlinelibrary.wiley.com/doi/10.1029/2024JA033285 by University Of Maryland, Wiley Online Library on [14/02/2025]. See the Terms and Conditions (https://onlinelibrary.wiley.com/terms-and-conditions) on Wiley Online Library for rules of use; OA articles are governed by the applicable Creative Commons License

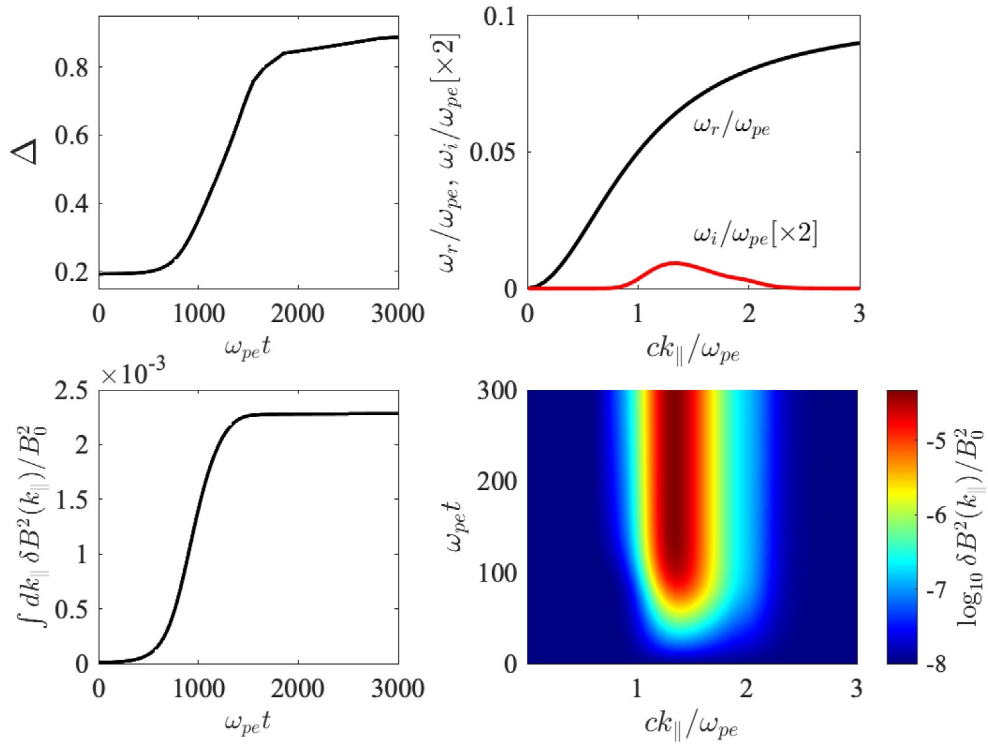

Figure 9. Numerical solution of Equation 17 and the self-consistent wave kinetic equation. The left-hand top panel shows the time evolution of shell spread parameter, Δ, and the left-hand bottom panel plots the integrated electromagnetic wave energy density, $\int dk_\parallel\, \delta B^2(k_\parallel)/B_0^2$, versus normalized time, $\omega_{pe}t$. The right-hand panels show the initial linear dispersion relation and the associated growth rate (top panel) and the dynamic spectrum (bottom panel).

$$
\begin{aligned}
\frac{d\Delta}{dt} &= \frac{8\pi^{\frac{1}{2}}e^2}{m_e^2\alpha^2 \mathrm{MN}}\int_0^\infty \frac{dk_\parallel}{k_\parallel\alpha}\,\delta E^2(k_\parallel)\int_0^\infty dy\left(\frac{3}{y+1}\right.\\
&\quad\left.+\frac{2(\Omega_e-\omega_r)(y+1)}{\omega_r}\right)\frac{(y+1)^2-1}{(y+1)^3}\,\eta_h\exp(-\zeta_h^2),\\
\eta_h &= \frac{\Omega_e-\omega_r}{k_\parallel\alpha}\left(\frac{(\Omega_e-\omega_r)(y+1)}{k_\parallel\alpha}-\frac{v_0}{\alpha}\right)-\frac{\eta^2}{(y+1)^3}-\frac{\Omega_e-\omega_r}{\omega_r}\frac{\eta^2}{y+1},\\
\zeta_h^2 &= \left(\frac{(\Omega_e-\omega_r)(y+1)}{k_\parallel\alpha}-\frac{v_0}{\alpha}\right)^2-\frac{\eta^2}{(y+1)^2},\\
M &= \frac{\eta^2\,\mathrm{erf}(\eta)}{\left(\eta e^{-\eta^2}\right)^2-\mathrm{erf}(\eta)\left[\pi^{\frac{1}{2}}\,\mathrm{erf}(\eta)-(1+2\eta^2)\eta e^{-\eta^2}\right]},\\
N &= ue^{-u^2}+\pi^{\frac{1}{2}}\left(\frac{1}{2}+u^2\right)[1+\mathrm{erf}(u)].
\end{aligned}
\tag{17}
$$

Numerical solution is shown in Figure 9. The pitch-angle spread parameter associated with the partial shell distribution, namely Δ, increases as the parallel whistler mode instability is excited [Figure 9, top-left panel]. This is consistent with our earlier findings (Yoon et al., 2019), in which the quasilinear analysis is compared against the 1D EM PIC simulation, except that now, we compare against the full 2D PIC simulation. The exponential increase of the wave energy density and the subsequent saturation is shown on the bottom-left panel of Figure 9. The dynamic spectrum is shown on the lower right panel, which can be compared against the simulation result, shown in Figure 4, bottom-left panel. Upon comparison against the PIC simulation, it can be seen that, while there is an overall favorable agreement, the quasilinear calculation predicts parallel wave numbers that are slightly higher

21699402, 2025, 2, Downloaded from https://agupubs.onlinelibrary.wiley.com/doi/10.1029/2024JA033285 by University Of Maryland, Wiley Online Library on [14/02/2025]. See the Terms and Conditions (https://onlinelibrary.wiley.com/terms-and-conditions) on Wiley Online Library for rules of use; OA articles are governed by the applicable Creative Commons License

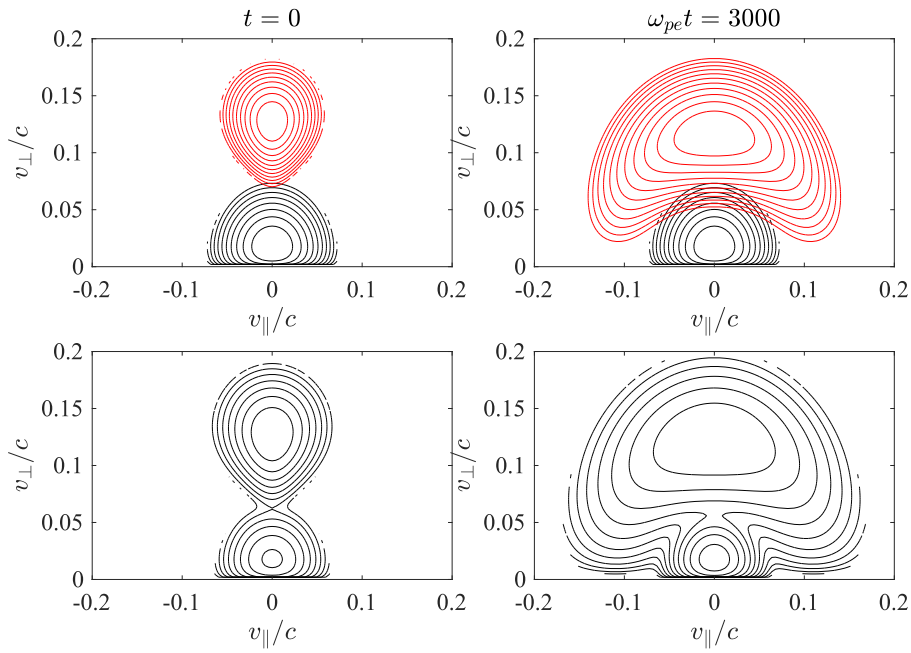

Figure 10. The evolution of initial thermal ring ([top and bottom] left) to a partial shell velocity distribution function at $\omega_{pe}t = 3000$ ([top and bottom] right) is captured by the quasilinear calculation based upon the model distribution (10). The top panels plot the partial distributions corresponding to the energetic ring-to-shell distribution and the background distribution separately, while the bottom panels plot the same results except that the two components are combined.

than that of the simulation result. Specifically, while the peak whistler-mode wave spectrum occurs in the range $1 < ck_\parallel/\omega_{pe} < 2$, according to the simulation, the peak intensity straddles the region defined by $ck_\parallel/\omega_{pe}sim1$. It can be seen that the most unstable mode predicted by the initial linear dispersive property, shown in Figure 9, upper-right panel, is accurately reflected in the dynamic spectrum. This is similar to the 2D PIC simulation result shown in Figure 4 that, the most unstable quasi-parallel mode in the 2D simulation takes place for $ck_\parallel/\omega_{pe}$ close to 1, or so, with the frequency in the close vicinity of the electron cyclotron frequency, which in the present case of $\omega_{pe}/\Omega_e = 10$, translated to $\omega \sim 0.1\omega_{pe}$.

The time scale of parallel whistler-mode instability excitation and saturation, which is around $\omega_{pe}t \sim 1000$, is also consistent with the 2D simulation result—see Figure 2. Unlike the electrostatic upper-hybrid mode, the quasi-parallel whistler mode does not show the reabsorption behavior according to the present 2D simulation. It is interesting that the present quasilinear analysis is consistent with the simulation in that, the wave energy density monotonically increases until saturation.

The reconstructed VDF at the end of calculation is shown in Figure 10. On the (top and bottom) left panels, the initial model based on the choice of $\Delta = 0.1925$ [Equation 11] is plotted, which demonstrates that with such a choice of Δ, the partial shell model quite accurately mimics the Gaussian thermal ring model—see Equation 1 and Figure 7. The top panels plot the contours of the ring and background distributions separately, while the bottom panels plot the same distribution except that the total distribution is shown—see Figure 8 for the same format. The evolved partial shell model at the end of computation, namely, $\omega_{pe}t = 3000$, is plotted on the (top and bottom) right-hand panels, where we have adopted the value $\Delta = 0.8856$, which is taken from the quasilinear calculation —see Figure 8, upper-left panel. The resulting reconstruction shown in Figure 10, is quite consistent with the simulated electron phase space distribution shown in Figures 5 and 6.

5. Summary and Discussion

Let us summarize the findings of the present paper. We have investigated the dynamical processes of the perpendicular velocity ring distribution of energetic electrons immersed in the background of protons and cold electrons as well as an ambient magnetic field. It was found that the ring electron distribution is unstable to the

21699402, 2025, 2, Downloaded from https://agupubs.onlinelibrary.wiley.com/doi/10.1029/2024JA033285 by University Of Maryland, Wiley Online Library on [14/02/2025]. See the Terms and Conditions (https://onlinelibrary.wiley.com/terms-and-conditions) on Wiley Online Library for rules of use; OA articles are governed by the applicable Creative Commons License

21699402, 2025, 2, Downloaded from https://agupubs.onlinelibrary.wiley.com/doi/10.1029/2024JA033285 by University Of Maryland, Wiley Online Library on [14/02/2025]. See the Terms and Conditions (https://onlinelibrary.wiley.com/terms-and-conditions) on Wiley Online Library for rules of use; OA articles are governed by the applicable Creative Commons License

combined upper-hybrid wave instability and the whistler-mode instability. The upper-hybrid waves excited by the ring electrons are characterized by a quasi perpendicular direction of propagation, and they are largely electrostatic. This instability operates during the early phase of the dynamical evolution, and the consequence is the reduction of the ring speed and a concomitant increase in the perpendicular thermal spread.

It was also found that the whistler-mode instability eventually becomes much more dominant during the later stage of the dynamical process. The whistler-mode waves are quasi parallel in terms of their direction of propagation, and is electromagnetic in nature with a right-hand circular polarization. The frequency range of the whistler-mode waves are of the order of electron cyclotron frequency, $\omega \sim \Omega_{ce}$, which is much lower than that of the upper-hybrid frequency, $\omega_{uh} = \sqrt{\omega_{pe}^2 + \Omega_{ce}^2} \sim \omega_{pe}$, which is roughly 10 times that of the electron cyclotron frequency under the present assumption of $\omega_{pe}/\Omega_{ce} = 10$. It was shown that the consequence of the longer-lasting whistler mode excitation is to cause the energetic ring electron distribution to undergo a pitch-angle diffusion such that the relaxed state corresponded to a partial velocity shell distribution.

We have analyzed the various properties of these two instabilities by performing detailed diagnostic tests, which included the various spectral analysis, and by carrying out the quasilinear analyses of these two instabilities to interpret the nature of these unstable wave excitation and the related electron relaxation process. It was shown that the early phase of instability was adequately explained by the quasilinear theory with the assumption of electrostatic mode propagating in the perpendicular direction, and with an additional assumption of the thermal ring electrons maintaining their essential mathematical form for their distribution function, except that the ring speed and perpendicular thermal spread increases in time. For the late phase of instability involving electromagnetic whistler waves, we employed another quasilinear theory with the assumption of exactly parallel propagation. By making an assumption of partial shell velocity distribution, we demonstrated that the simple 1D quasilinear theory captured the essential aspects of the dynamical evolution. This showed that the quasilinear theory is a useful first order theory, which could be used for other applications.

It should be noted that the 2D quasilinear that encompasses both the early phase upper-hybrid mode dynamics and the later phase whistler-mode dynamics is not yet available. The main difficulty associated with such a general quasilinear theory stems from the challenging aspect of locating (or modeling) the quasi-perpendicular extensions of the multiple-harmonic cyclotron modes, which includes the upper-hybrid mode. For exactly perpendicular angle of propagation, the dispersion relation (Equation 4), while quite complicated, nevertheless can be turned into a polynomial equation upon truncating the infinite harmonic series, which can readily be solved by a numerical root solving routine. Once the mode propagating angle deviates from the exactly 90° angle, however, the more general dispersion relation becomes a transcendental equation involving the plasma dispersion function,

$$0 = 1 + \frac{2\omega_{pe}^2}{k^2\alpha_e^2}\left(1 + \sum_{n=-\infty}^{\infty} I_n(\lambda)\, e^{-\lambda}\, \xi Z(\zeta_n)\right),$$
$$\xi = \frac{\omega}{k_\parallel \alpha_e}, \qquad \zeta_n = \frac{\omega - n\Omega_e}{k_\parallel \alpha_e}, \tag{18}$$

whose complex roots must be solved carefully. In Equation 18 various quantities are already defined in Equation 4, except for the plasma dispersion function, which is defined by $Z(\zeta) = \pi^{-1/2}\int_{-\infty}^{\infty}(x - \zeta)^{-1}e^{-x^2}dx$, for $\mathrm{Im}(\zeta) > 0$.

Among the findings that cannot be explained within the theoretical framework of quasilinear includes the excitation of the harmonic upper-hybrid waves seen in Figure 4. This feature was highly reminiscent of the harmonic Langmuir waves observed in the beam-plasma simulations in unmagnetized plasmas (Gaelzer et al., 2003; Li et al., 2021; Umeda et al., 2003; Yoon et al., 2003).

Data Availability Statement

The theoretical plots are in normalized units, and the equations are clearly explained in the text. Therefore, no actual data are generated by the theory. The simulation results presented in this study are publicly available at Zenodo (Lee & Yoon, 2025).

Acknowledgments
P. H. Y. was supported by NASA Grant 80NSSC19K0827, NSF Grant 2203321, and the Department of Energy (DOE DE-SC0022963) through the NSF/DOE Partnership in Basic Plasma Science and Engineering.

References

Artemyev, A., Agapitov, O., Mourenas, D., Krasnoselskikh, V., Shastun, V., & Mozer, F. (1978). Oblique whistler-mode waves in the Earth's inner magnetosphere: Energy distribution, origins, and role in radiation belt dynamics. *Space Science Reviews*, *200*(1–4), 261–355. https://doi.org/10.1007/s11214-016-0252-5

Christiansen, P., Gough, P., Martelli, G., Bloch, J.-J., Cornilleau, N., Etcheto, J., et al. (1978a). Geos I: Identification of natural magnetospheric emissions. *Nature*, *272*(5655), 682–686. https://doi.org/10.1038/272682a0

Christiansen, P. J., Gough, M. P., Martelli, G., Bloch, J. J., Cornilleau, N., Etcheto, J., et al. (1978b). Geos-I observations of electrostatic waves, and their relationship with plasma parameters. *Space Science Reviews*, *22*(4), 383. https://doi.org/10.1007/bf00210875

Cully, C. M., Bonnell, J. W., & Ergun, R. E. (2008). THEMIS observations of long-lived regions of large-amplitude whistler waves in the inner magnetosphere. *Journal of Geophysical Research*, *35*(17), L17S16. https://doi.org/10.1029/2008GL033643

Davidson, G., & Walt, M. (1977). Loss cone distributions of radiation belt electrons. *Journal of Geophysical Research*, *82*(1), 48–54. https://doi.org/10.1029/JA082i001p00048

Davidson, R. C. (1972). *Methods in nonlinear plasma theory*. Academic Press.

Eliasson, B., Speirs, D. C., & Daldorff, L. K. S. (2016). Electrostatic electron cyclotron instabilities near the upper hybrid layer due to electron ring distributions. *Plasma Physics and Controlled Fusion*, *58*(9), 095002. https://doi.org/10.1088/0741-3335/58/9/095002

Gaelzer, R., Yoon, P. H., Umeda, T., Omura, Y., & Matsumoto, H. (2003). Harmonic Langmuir waves: II. Turbulence spectrum. *Physics of Plasmas*, *10*(2), 373–381. https://doi.org/10.1063/1.1537239

Gary, S. P., & Wang, J. (1996). Whistler instability: Electron anisotropy upper bound. *Journal of Geophysical Research*, *101*(A5), 10749–10754. https://doi.org/10.1029/96JA00323

Grach, S. M. (1999). On kinetic effects in the ionospheric F-region modified by powerful radio waves. *Radophysics and Quantum Electronics*, *42*(7), 572–588. https://doi.org/10.1007/bf02677563

Helliwell, R. A. (1969). Low-frequency waves in the magnetosphere. *Reviews of Geophysics*, *7*(1–2), 281–303. https://doi.org/10.1029/RG007i001p00281

Kurth, W. S., Ashour-Abdalla, M., Frank, L. A., Kennel, C. F., Gurnett, D. A., Sentman, D. D., & Burek, B. G. (1979). A comparison of intense electrostatic waves near f_{UHR} with linear instability theory. *Geophysical Research Letters*, *6*, 487–490. https://doi.org/10.1029/GL006i006p00487

Kurth, W. S., Craven, J. D., Frank, L. A., & Gurnett, D. A. (1979). Intense electrostatic waves near the upper hybrid resonance frequency. *Journal of Geophysical Research*, *84*(A8), 4145–4164. https://doi.org/10.1029/JA084iA08p04145

Kurth, W. S., De Pascuale, S., Faden, J. B., Kletzing, C. A., Hospodarsky, G. B., Thaller, S., & Wygant, J. R. (2015). Electron densities inferred from plasma wave spectra obtained by the wave instrument on Van Allen Probes. *Journal of Geophysical Research*, *120*(2), 904–914. https://doi.org/10.1002/2014JA020857

LaBelle, J., & Treumann, R. A. (1988). Plasma waves at the dayside magnetopause. *Space Science Reviews*, *47*(1–2), 175. https://doi.org/10.1007/BF00223240

LaBelle, J. & Treumann, R. A. (Eds.) (2006)., *Geospace electromagnetic waves and radiation*. Springer. https://doi.org/10.1007/b11580119

LaBelle, J., Weatherwax, A. T., Tantiwiwat, M., Jackson, E., & Linder, J. (2005). Statistical studies of auroral MF burst emissions observed at South Pole Station and at multiple sites in northern Canada. *Journal of Geophysical Research*, *110*(A2), A02305. https://doi.org/10.1029/2004JA010608

Lee, J., Yoon, P. H., Seough, J., López, R. A., Hwang, J., Lee, J., & Choe, G. S. (2018). Simulation and quasi-linear theory of magnetospheric Bernstein mode instability. *Journal of Geophysical Research: Space Physics*, *123*(9), 7320–7331. https://doi.org/10.1029/2018JA025667

Lee, S.-Y., Lee, E., Kim, K.-H., Seon, J., Lee, D.-H., & Ryu, K.-S. (2015). Development and test of 2.5-dimensional electromagnetic PIC simulation code. *Journal of Astronomy and Space Sciences*, *32*(1), 45–50. https://doi.org/10.5140/JASS.2015.32.1.45

Lee, S.-Y., Yi, S., Lim, D., Kim, H.-E., Seough, J., & Yoon, P. H. (2013). Loss cone-driven cyclotron maser instability. *Journal of Geophysical Research: Space Physics*, *118*(11), 7036–7044. https://doi.org/10.1002/2013JA019298

Lee, S.-Y., & Yoon, P. H. (2025). Excitation of upper-hybrid and whistler-mode waves by electron velocity ring distribution [Dataset]. *Zenodo*. https://zenodo.org/records/14649009

Li, T. M., Li, C., Chen, P. F., & Ding, W. J. (2021). Particle-in-cell simulation of plasma emission in solar radio bursts. *Astronomy & Astrophysics*, *653*, A169. https://doi.org/10.1051/0004-6361/202140973

Li, W. Y., Graham, D. B., Khotyaintsev, Y. V., Vaivads, A., André, M., Min, K., et al. (2020). Electron Bernstein waves driven by electron crescents near the electron diffusion region. *Nature Communications*, *11*(1), 141. https://doi.org/10.1038/s41467-019-13920-w

Ma, Q., Li, W., Zhang, X.-J., Bortnik, J., Shen, X.-C., Daly, A., et al. (2024). Generation and impacts of whistler-mode waves during energetic electron injections in Jupiter's outer radiation belt. *Journal of Geophysical Research*, *129*(7), e2024JA032624. https://doi.org/10.1029/2024JA032624

Matsumoto, H., & Usui, H. (1997). Intense bursts of electron cyclotron harmonic waves near the daysude magnetosphere observed by GEOTAIL. *Geophysical Research Letters*, *24*(1), 49–52. https://doi.org/10.1029/96GL03650

Menietti, J. D., Averkamp, T. F., Imai, M., Kurth, W. S., Clark, G. B., Allegrini, F., et al. (2021). Low-latitude whistler-mode and higher-latitude Z-mode emission at Juipter observed by Juno. *Journal of Geophysical Research*, *126*(2), e2020JA028742. https://doi.org/10.1029/2020JA028742

Ni, S., Chen, Y., Ki, C., Zhang, Z., Ning, H., Kong, X., et al. (2020). Plasma emission induced by electron cyclotron maser instability in solar plasmas with a large ratio of plasma frequency to gyrofrequency. *The Astrophysical Journal Letters*, *891*, L25. https://doi.org/10.3847/2041-8213/ab7750

Pritchett, P. L. (1984a). Relativistic dispersion and the generation of auroral kilometric radiation. *Geophysical Research Letters*, *11*(2), 143–146. https://doi.org/10.1029/GL011i002p00143

Pritchett, P. L. (1984b). Relativistic dispersion, the cyclotron maser instability, and auroral kilometric radiation. *Journal of Geophysical Research*, *89*(A10), 8957–8970. https://doi.org/10.1029/JA089iA10p08957

Pritchett, P. L. (1986). Electron-cyclotron maser instability in relativistic plasmas. *Physics of Fluids*, *29*(9), 2919–2930. https://doi.org/10.1063/1.865492

Pritchett, P. L. (1999). Free energy sources and frequency bandwidth for the auroral kilometric radiation. *Journal of Geophysical Research*, *104*(A5), 10–317. https://doi.org/10.1029/1998JA900179

Pritchett, P. L., & Strangeway, R. J. (1985). A simulation study of kilometric radiation generation along an auroral field line. *Journal of Geophysical Research*, *90*(A10), 9650–9662. https://doi.org/10.1029/JA090iA10p09650

21699402, 2025, 2, Downloaded from https://agupubs.onlinelibrary.wiley.com/doi/10.1029/2024JA033285 by University Of Maryland, Wiley Online Library on [14/02/2025]. See the Terms and Conditions (https://onlinelibrary.wiley.com/terms-and-conditions) on Wiley Online Library for rules of use; OA articles are governed by the applicable Creative Commons License

Pritchett, P. L., & Winglee, R. M. (1989). Generation and propagation of kilometric radiation in the auroral plasma cavity. *Journal of Geophysical Research*, *94*(A1), 129–143. https://doi.org/10.1029/JA094iA01p00129

Ram, A. K., Bers, A., & Lashmore-Davies, C. N. (2002). Emission of electron Bernstein waves in plasmas. *Physics of Plasmas*, *9*(2), 409–418. https://doi.org/10.1063/1.1429634

Sagdeev, R. Z., & Galeev, A. A. (1969). *Nonlinear plasma theory*. Benjamin.

Summers, D., Ma, C., & Mukai, T. (2004). Competition between acceleration and loss mechanisms of relativistic electrons during geomagnetic storms. *Journal of Geophysical Research*, *109*(A4), A04221. https://doi.org/10.1029/2004JA010437

Thorne, R., Ni, B., Tao, X., & Meredith, N. P. (2010). Scattering by chorus waves as the dominant cause of diffuse auroral precipitation. *Nature*, *467*(7318), 943–946. https://doi.org/10.1038/nature09467

Umeda, T., Ashour-Abdalla, M., Schriver, D., Richard, R. L., & Coroniti, F. V. (2007). Particle-in-cell simulation of Maxwellian ring velocity distribution. *Journal of Geophysical Research*, *112*(A4), A04212. https://doi.org/10.1029/2006JA012124

Umeda, T., Omura, Y., Yoon, P. H., Gaelzer, R., & Matsumoto, H. (2003). Harmonic Langmuir waves: III. Vlasov simulation. *Physics of Plasmas*, *10*(2), 382–391. https://doi.org/10.1063/1.1537240

Usui, H., Paterson, W. R., Matsumoto, H., Frank, L. A., Nakamura, M., Matsui, H., et al. (1999). Geotail electron observations in association with intense bursts of electron cyclotron harmonic waves in the dayside magnetosphere. *Journal of Geophysical Research*, *104*, 4477.

Weatherwax, A. T., LaBelle, J., Trimpi, M. L., Treumann, R. A., Minow, J., & Deehr, C. (1995). Statistical and case studies of radio emissions observed near $2f_{ce}$ and $3f_{ce}$ in the auroral zone. *Journal of Geophysical Research: Space Physics*, *100*(A5), 7745–7757. https://doi.org/10.1029/94JA03147

Wu, C. S., & Lee, L. C. (1979). A theory of the terrestrial kilometric radiation. *The Astrophysical Journal*, *230*, 621. https://doi.org/10.1086/157120

Wu, C. S., Yoon, P. H., & Li, Y. (2000). A new scenario for type III solar radio emission. *The Astrophysical Journal*, *540*(1), 572–582. https://doi.org/10.1086/309308

Yoon, P. H., Gaelzer, R., Umeda, T., Omura, Y., & Matsumoto, H. (2003). Harmonic Langmuir waves: I. Nonlinear dispersion relation. *Physics of Plasmas*, *10*(2), 364–372. https://doi.org/10.1063/1.1537238

Yoon, P. H., Lee, J., Hwang, J., Seough, J., & Choe, G. S. (2019). Whistler instability driven by electron thermal ring distribution with magnetospheric application. *Journal of Geophysical Research: Space Physics*, *124*(7), 5289–5301. https://doi.org/10.1029/2019JA026687

Yoon, P. H., & Omura, Y. (2023). Electrostatic upper-hybrid mode instability driven by a ring electron distribution. *Physics of Plasmas*, *30*(6), 062107. https://doi.org/10.1063/5.0151710

Yoon, P. H., Wu, C. S., & Wang, C. B. (2002). Generation of type III solar radio bursts in the low corona by direct amplification. II. Further numerical study. *The Astrophysical Journal*, *576*(1), 552–560. https://doi.org/10.1086/341634

Zhang, X.-J., Ma, Q., Artemyev, A. V., Li, W., Kurth, W. S., Mauk, B. H., et al. (2020). Plasma sheet boundary layer in Jupiter's magnetodisk as observed by Juno. *Journal of Geophysical Research*, *125*(8), e2020JA027957. https://doi.org/10.1029/2020JA027957

21699402, 2025, 2, Downloaded from https://agupubs.onlinelibrary.wiley.com/doi/10.1029/2024JA033285 by University Of Maryland, Wiley Online Library on [14/02/2025]. See the Terms and Conditions (https://onlinelibrary.wiley.com/terms-and-conditions) on Wiley Online Library for rules of use; OA articles are governed by the applicable Creative Commons License